International Journal of Heat and Mass Transfer 173 (2021) 121217

Contents lists available at ScienceDirect

International Journal of Heat and Mass Transfer

journal homepage: www.elsevier.com/locate/hmt

Instabilities of thermocapillary liquid layers with two free surfaces

Kai-Xin Hu[a,*], Cheng-Zhuo Zhao[a], Shao-Neng Zhang[a], Qi-Sheng Chen[b,c]

[a] Key Laboratory of Impact and Safety Engineering (Ministry of Education), School of Mechanical Engineering and Mechanics, Ningbo University, Ningbo, Zhejiang 315211, China
[b] School of Engineering Science, University of Chinese Academy of Sciences, Beijing 100190, China
[c] Key Laboratory of Microgravity, Institute of Mechanics, Chinese Academy of Sciences, Beijing 100190, China

ARTICLE INFO

Article history:
Received 6 January 2021
Revised 6 March 2021
Accepted 11 March 2021
Available online 26 March 2021

ABSTRACT

The instabilities of thermocapillary liquid layers with two free surfaces are examined by linear stability analysis. The surface tension is big enough to keep the liquid surfaces non-deformable. The effect of vertical temperature difference between two interfaces (Q) is considered. The critical parameters of preferred modes are determined, which depend on the Prandtl number (Pr) and Biot number (Bi). When Q=0, the preferred modes are the oblique wave at small Pr and the streamwise wave at large Pr. The perturbation is symmetric and anti-symmetric at small and large Pr, respectively. When $Q>0$, the preferred mode changes from the oblique wave to the streamwise wave, and finally the spanwise stationary mode with the increase of Pr. The instability mechanism is discussed. Comparisons are made with the liquid layer with a single free surface and previous results by numerical simulations and experiments.

© 2021 Elsevier Ltd. All rights reserved.

1. Introduction

Thermocapillary convection refers to the fluid motion driven by the temperature-induced surface tension gradient. It has received much attention due to its great practical importance in crystal growth [1], inkjet printing [2], droplet migration [3], microfluidics [4] and additive manufacturing [5]. The flow becomes unstable once the temperature gradient exceeds a threshold. A great deal of theoretical and experimental works on thermocapillary instabilities have been carried out in the last four decades, which have been reviewed by Davis [6], Schatz & Neitzel [7] and Lappa [8].

In theoretical studies, the model of thermocapillary liquid layer proposed by Smith & Davis [9] is widely used. They suggest that there are two kinds of thermocapillary instabilities. The first one is the convective instability, which is driven by mechanisms within the bulk of the layer and does not depend on the surface deformation [6]. The stationary rolls and travelling waves of convective instability predicted by the modal stability theory have been observed in both experiments [10] and numerical simulations [11]. The energy analysis shows the convective instability at small Prandtl number (Pr) is purely hydrodynamic, while that at large Pr is hydrothermal [12–13].

The second one is related to the surface deformation. Smith & Davis [14] have considered the two-dimensional traveling waves that couple the interfacial deflection to the underlying shear flow. It was found that the surface-wave instability is most prominent at low Pr and hydrodynamic in nature [6]. This work has been generalized to three-dimensional waves by Patne, Agnon & Oron [15]. The general linear stability analysis they performed reveals a stabilization effect of the imposed horizontal component of the oblique temperature gradient (OTG) on the long-wave instabilities introduced by the vertical component of the OTG.

In recent years, some authors have investigated thermocapillary instabilities in some new fields, such as non-Newtonian fluid flows [16–19], the layer on an inclined plane [13], non-modal stability [20], droplet migration [21], sideband thermocapillary instability [22] and bifurcation routes to chaos [23–24]. However, the above works mainly focus on the liquid layer with a solid boundary, which only has a single free surface.

There have been a few studies devoted to the thermocapillary instability in the liquid layer with two free surfaces. NASA astronaut Pettit [25] has performed a series of microgravity experiments of oscillatory thermocapillary flows on the International Space Station, where a liquid film of water in a ring is exposed to a non-uniform temperature distribution. These experiments suggest that the free liquid film has a potential to obtain a new kind of crystallization process of materials [26]. Ueno & Torii [27] have examined the thermocapillary-driven flow in a thin liquid film sustained in a rectangular hole by numerical and experimental approaches. Limsukhawat et al. [28] have performed three-dimensional numerical simulations on a thermocapillary-driven flow in a free liquid film sustained in a hole. Messmer et al. [29] have reported the exper-

* Corresponding author.
E-mail address: hukaixin@nbu.edu.cn (K.-X. Hu).

https://doi.org/10.1016/j.ijheatmasstransfer.2021.121217
0017-9310/© 2021 Elsevier Ltd. All rights reserved.

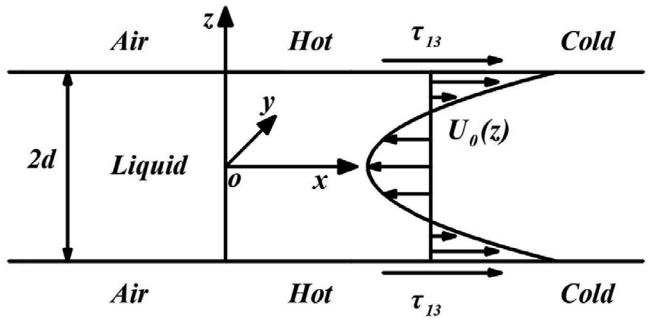

Fig. 1. Schematic of the thermocapillary liquid layer with two free surfaces. Here, d is half the depth of layer, τ_{13} is the shear stress on the surface and U_0 is the velocity field.

iments on double free-surface films with thermocapillary forcing, which show two basic flow structures at low Marangoni Numbers. Yamamoto et al. [30–31] have carried out numerical simulations of oscillatory thermocapillary flows under zero gravity in a circular liquid film with concave free surfaces. They found that the water film geometry is an important parameter and gives rise to three oscillatory flow structures in the film. Watanabe, Kowata & Ueno [26] have experimentally investigated the thermocapillary-driven flow in a free liquid film with two gas-liquid interfaces, which shows that the flow exhibits a transition from the two-dimensional steady flow state to the three-dimensional oscillatory state. The above works have presented many unique flow patterns which cannot be found in the layer with a single free surface.

However, to the best of our knowledge, the stability of thermocapillary layer with two free surfaces has not been discussed theoretically. The instability mechanism in such flows is also not well understood. In order to study its physical properties and mechanism, we perform three-dimensional linear stability analysis on the convective instability in the thermocapillary layer with two gas-liquid interfaces in this paper. The temperature difference between two interfaces is considered. The results at different Prandtl numbers and Biot numbers are presented.

The paper is organized as follows. The physical model and mathematical formulations are presented in Section 2. The dimensionless governing equations and boundary conditions are derived. Section 3 is dedicated to the modal analysis. The preferred modes are displayed and the energy mechanism is studied. Then, Section 4 is devoted to the instability mechanism and comparisons with previous works. Finally, the conclusions are summarized in Section 5.

2. Problem formulation

We consider the thermocapillary liquid layer displayed in Fig. 1, where a layer with two free surfaces is subjected to a constant temperature gradient $b = -\mathrm{d}T/\mathrm{d}x > 0$ on its upper and lower surfaces. We choose the reference frame where the flux in the x direction is zero. x, y, z are the streamwise, spanwise and normal direction, respectively. The surface tension $\hat{\sigma}$ changes with the temperature T as $\hat{\sigma} = \hat{\sigma}_0 - \gamma(T - T_0)$, where $\gamma = -\mathrm{d}\hat{\sigma}/\mathrm{d}T > 0$. Thus, a convection is driven by the Marangoni forces on the free surfaces while the surface tension is big enough to keep two surfaces flat.

2.1. Governing equations

Suppose the liquid is an incompressible Newtonian fluid, whose viscosity E_k, density 3.37×10^5, thermal diffusivity 4.10×10^3, thermal conductivity E_T and unit thermal surface conductance 2.74×10^{-4} are constants. We choose the scales of length, velocity, stress and temperature difference as d, $\hat{U}_0 = b\gamma d/\mu$, γb and bd, respectively. The Reynolds number, Marangoni number, Prandtl number and Biot number are defined as $R = \rho\hat{U}_0 d/\mu$, $Ma = b\gamma d^2/(\mu\chi)$, $Pr = \mu/(\rho\chi)$ and $Bi = \hat{h}d/\hat{k}$, respectively. The relation between Ma and R is: $Ma = R \cdot Pr$.

The dimensionless governing equations are given below, which are the continuity equation, momentum equation and energy equation, respectively.

$$\nabla \cdot \mathbf{u} = 0, \tag{2.1}$$

$$R\left(\frac{\partial \mathbf{u}}{\partial t} + \mathbf{u} \cdot \nabla \mathbf{u}\right) = -\nabla p + \nabla \cdot \boldsymbol{\tau}, \tag{2.2}$$

$$\frac{\partial T}{\partial t} + \mathbf{u} \cdot \nabla T = \frac{1}{Ma}\nabla^2 T. \tag{2.3}$$

Here, $\mathbf{u}$, p, T and $\boldsymbol{\tau}$ stand for the velocity, pressure, temperature and stress tensor, respectively. For Newtonian fluid,

$$\boldsymbol{\tau} = \mathbf{S}, \tag{2.4}$$

where $\mathbf{S} = \nabla\mathbf{u} + (\nabla\mathbf{u})^{\mathrm{T}}$ is the strain-rate tensor.

In the present work, we neglect the surface deformation and restrict our attention to the convective instability. The magnitude of the surface deformation can be measured by the capillary number: $Ca = \mu\hat{U}_0/\hat{\sigma}_0$. The assumption of non-deformable surfaces is reasonable when $Ca << 1$. In reality, this can be satisfied for many liquid layers, such as the liquid silicon [9] (Pr=0.023, $O(Ca) \approx 10^{-4}$) and the silicone oil [10] (Pr=13.9, $O(Ca) \approx 10^{-3}$).

The boundary conditions of stress and velocity on the upper surface ($z = 1$) are

$$\tau_{13} + \frac{\partial T}{\partial x} = 0, \tau_{23} + \frac{\partial T}{\partial y} = 0, w = 0. \tag{2.5a}$$

Here, the first two equations stand for the relation between the temperature gradient and the shear stress caused by thermocapillary effect [6], while the last is due to no surface deformation. The balance of heat flux on the surface leads to [9]

$$-\frac{\partial T}{\partial z} = Bi \cdot (T - T_\infty^{\mathrm{u}}) + \tilde{Q}_1. \tag{2.5b}$$

Similar equations can be obtained on the lower surface ($z = -1$),

$$\tau_{13} - \frac{\partial T}{\partial x} = 0, \tau_{23} - \frac{\partial T}{\partial y} = 0, w = 0, \tag{2.5c}$$

$$\frac{\partial T}{\partial z} = Bi \cdot \left(T - T_\infty^{\mathrm{d}}\right) + \tilde{Q}_2. \tag{2.5d}$$

Here, $T_\infty^{\mathrm{u}}, T_\infty^{\mathrm{d}}$ are the temperatures of bounding gas near the upper and lower surfaces, respectively. $\tilde{Q}_1, \tilde{Q}_2$ are the imposed heat fluxes to the environment, which are introduced for the energy balance and can be determined by the basic-state solution.

We assume that the basic flow is fully developed, so the velocity distribution of basic flow is parallel while the temperature is linear in x plus a distribution in z,

$$\mathbf{u} = (U_0(z), 0, 0), T_0(x, z) = -x + T_b(z). \tag{2.6a}$$

Here, the subscript 0 stands for the basic flow and T_b is the vertical temperature distribution. Similar to the layer in Ref. [9], $T_\infty^{\mathrm{u}}, T_\infty^{\mathrm{d}}$ have

$$T_\infty^{\mathrm{u}} = -x + T_b(1), T_\infty^{\mathrm{d}} = -x + T_b(-1). \tag{2.6b}$$

Substituting (2.6) into governing equations, the solutions of the basic flow can be derived as $U_0(z) = C_1 z^2 + C_2 z + C_3$, where C_1, C_2, C_3 are constants. Because γb is chosen as the scale of stress, the dimensionless value of shear stress on the upper surface $\tau_{13}(1)$ for

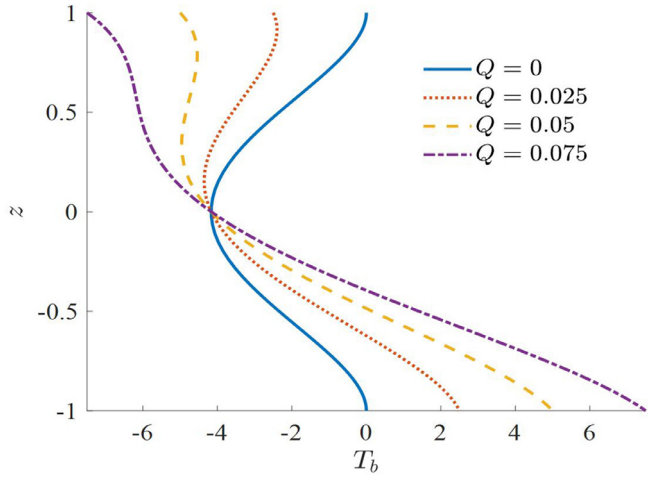

Fig. 2. The temperature distributions in the vertical direction for basic flow at Ma=100.

the basic flow is 1, which can also be derived by substituting the second equation of (2.6a) into the first equation of (2.5a). Thus, the boundary conditions of velocity U_0 are $DU_0(1) = 1 = -DU_0(-1)$, where $D = \mathrm{d}/\mathrm{d}z$. In addition, there is zero mass flux in the vertical section $\int_0^1 U_0(z)\mathrm{d}z = 1$. Then, the solution of $U_0(z)$ can be determined in (2.7). $T_b(z)$ is obtained in (2.8) by the equation $-U_0(z) = \frac{1}{Ma}D^2T_b(z)$ and its boundary conditions in (2.5).

$$U_0(z) = \frac{1}{2}\left(z^2 - \frac{1}{3}\right), \tag{2.7}$$

$$T_b(z) = Ma\left(-\frac{1}{24}z^4 + \frac{1}{12}z^2 - \frac{1}{24} - Qz\right), \tag{2.8}$$

Here, $Q = \frac{T_\infty^{\mathrm{d}} - T_\infty^{\mathrm{u}}}{2Ma}$ is a measure of vertical temperature difference between two surfaces and we assume that $T_b(1) = 0$ when $Q = 0$. Finally, $\tilde{Q}_1, \tilde{Q}_2$ are derived by (2.5),

$$\tilde{Q}_1 = -\tilde{Q}_2 = MaQ. \tag{2.9}$$

The distributions of velocity and temperature are displayed in Figs. 1&2. It can be seen that when $Q = 0$, T_b is symmetric with respect to z=0 and the surface is hotter than the interior. The increase of Q leads to the asymmetry of T_b. When $Q \geq 0.075$, T_b always decrease with z.

2.2. Modal analysis

Suppose an infinitesimal perturbation in the normal mode form is added to the basic flow,

$$(\mathbf{u}, T, P, \boldsymbol{\tau}) = (\mathbf{u}_0, T_0, P_0, \boldsymbol{\tau}_0) + \boldsymbol{\delta}, \tag{2.10a}$$

$$\boldsymbol{\delta} = \left(\hat{u}, \hat{v}, \hat{w}, \hat{T}, \hat{P}, \hat{\tau}\right)\exp\left[i(-\omega t + \alpha x + \beta y)\right]. \tag{2.10b}$$

Hereafter, the variables without subscript 0 stand for the perturbation. The mode has a complex frequency $\omega = \omega_r + \mathrm{i}\omega_i$ and the wave numbers α, β in the x and y directions, respectively. The total wave number $k = \sqrt{\alpha^2 + \beta^2}$ and the propagation angle $\theta = \tan^{-1}(\beta/\alpha)$ are used in the following. $\psi = -\omega t + \alpha x + \beta y$ is the perturbation phase and $c = |\omega_r|/k$ is the phase speed of perturbation wave.

We can obtain the linearized perturbation equations by substituting (2.10) into the governing equations (2.1)-(2.4) and boundary conditions (2.5),

$$i\alpha\hat{u} + i\beta\hat{v} + D\hat{w} = 0, \tag{2.11}$$

$$\begin{aligned} &R\left[\beta\left(\hat{w}DU_0 + U_0 i\alpha\hat{u}\right) - \alpha\left(U_0 i\alpha\hat{v}\right)\right] \\ &-\beta\left(i\alpha\hat{\tau}_{11} + i\beta\hat{\tau}_{12} + D\hat{\tau}_{13}\right) + \alpha\left(i\alpha\hat{\tau}_{12} + i\beta\hat{\tau}_{22} + D\hat{\tau}_{23}\right) \\ &= Ri\omega\left(\beta\hat{u} - \alpha\hat{v}\right), \end{aligned} \tag{2.12}$$

$$\begin{aligned} &R\alpha\left(D\hat{w}\cdot DU_0 + \hat{w}D^2U_0 + DU_0\cdot i\alpha\hat{u} + U_0 i\alpha D\hat{u}\right) \\ &+R\beta\left(DU_0\cdot i\alpha\hat{v} + U_0 i\alpha D\hat{v}\right) - Rik^2\left(U_0 i\alpha\hat{w}\right) \\ &-\left(i\alpha^2 D\hat{\tau}_{11} + 2i\alpha\beta D\hat{\tau}_{12} + \alpha D^2\hat{\tau}_{13} + i\beta^2 D\hat{\tau}_{22} + \beta D^2\hat{\tau}_{23}\right) \\ &+ik^2\left(i\alpha\hat{\tau}_{13} + i\beta\hat{\tau}_{23} + D\hat{\tau}_{33}\right) \\ &= Ri\omega\left(\alpha D\hat{u} + \beta D\hat{v} - ik^2\hat{w}\right), \end{aligned} \tag{2.13}$$

$$Ma\left(\hat{u}\frac{\partial T_0}{\partial x} + \hat{w}\frac{\partial T_0}{\partial z} + U_0 i\alpha\hat{T}\right) + \left(\alpha^2 + \beta^2\right)\hat{T} - D^2\hat{T} = Mai\omega\hat{T}, \tag{2.14}$$

$$\hat{\tau}_{11} - 2i\alpha\hat{u} = 0, \tag{2.15a}$$

$$\hat{\tau}_{22} - \left(2i\beta\hat{v}\right) = 0, \tag{2.15b}$$

$$\hat{\tau}_{13} + i\alpha\hat{T} = 0, \hat{\tau}_{23} + i\beta\hat{T} = 0, \hat{w} = 0, D\hat{T} + Bi\hat{T} = 0, z = 1. \tag{2.16}$$

$$\hat{\tau}_{13} - i\alpha\hat{T} = 0, \hat{\tau}_{23} - i\beta\hat{T} = 0, \hat{w} = 0, D\hat{T} - Bi\hat{T} = 0, z = -1. \tag{2.17}$$

Indeed, (2.12) & (2.13) are obtained by eliminating $\hat{p}$ from the following equations, which are three components of the momentum equation,

$$R\left(-i\omega\hat{u} + \hat{w}DU_0 + U_0 i\alpha\hat{u}\right) = -i\alpha\hat{p} + i\alpha\hat{\tau}_{11} + i\beta\hat{\tau}_{12} + D\hat{\tau}_{13}, \tag{2.18}$$

$$R(-i\omega\hat{v} + U_0 i\alpha\hat{v}) = -i\beta\hat{p} + i\alpha\hat{\tau}_{12} + i\beta\hat{\tau}_{22} + D\hat{\tau}_{23}, \tag{2.19}$$

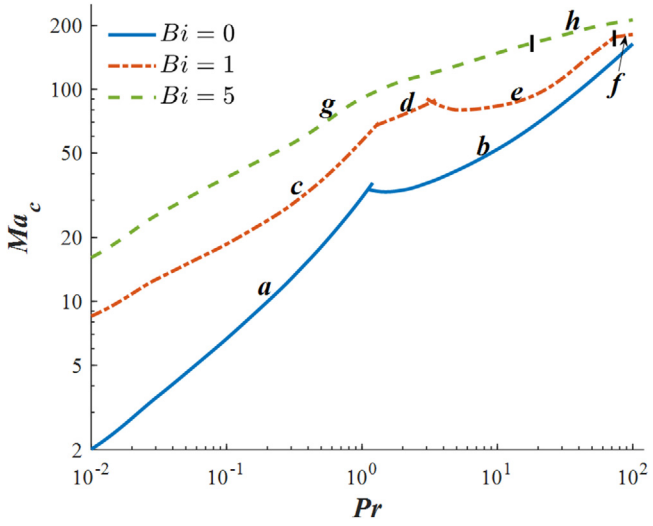

Fig. 3. The variation of Ma_c with Pr at Q=0.The curves correspond to oblique waves: (a), (c), (d), (g); and streamwise waves: (b), (e), (f), (h). Both axes are logarithmic.

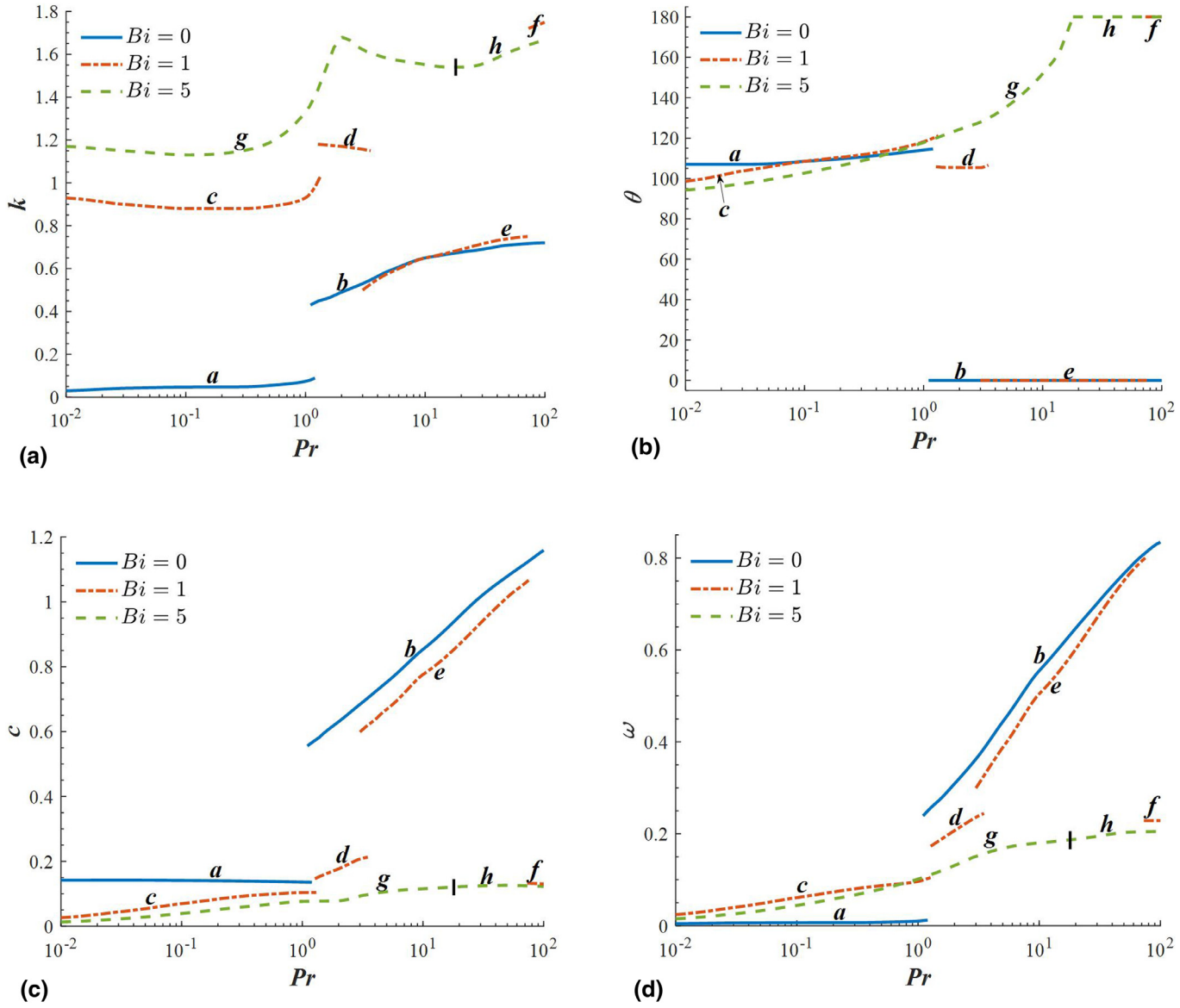

Fig. 4. The (I) wave number, (II) wave propagation angle, (III) wave speed and (IV) frequency corresponding to the modes in Fig. 3.

$$R\left(-i\omega\bar{w}+U_0 i\alpha\bar{w}\right)=-D\bar{p}+i\alpha\bar{\tau}_{13}+i\beta\bar{\tau}_{23}+D\bar{\tau}_{33}. \tag{2.20}$$

We compute ω numerically by the Chebyshev collocation method [32], where N_c Gauss-Lobatto points are set in the flow region $z=\cos(\frac{j\pi}{N_c+1})$, $j=1\sim N_c$ while 2 points $z=\pm1$ are set at the boundaries. The perturbation quantities are expanded in Chebyshev polynomials, such as

$$\bar{w}=\sum_{j=1}^{N_c+2}a_j H_{j-1}(z), \tag{2.21}$$

where $H_{j-1}(z)=\cos((j-1)\cos^{-1}(z))$ is the $(j-1)$−th Chebyshev polynomial and a_j is the coefficient. Substituting these Chebyshev polynomials into (2.11)-(2.17), we can write the perturbation equations in the form of $\mathbf{Wg}=\omega\mathbf{Zg}$, where $\mathbf{W},\mathbf{Z}$ are two matrices, ω is the eigenvalue and $\mathbf{g}=(a_1,a_2...,a_{10N_C+8})^{\mathrm{T}}$ is the eigenvector of coefficients. The eigenvalues are obtained by using the QZ algorithm available in the Matlab-software package [33]. In present work, the results are sufficiently accurate when 80~120 Chebyshev nodes are used.

In order to valid our code, we have computed some critical parameters of thermocapillary liquid layers with a single free surface, which can be realized by changing the boundary condition of the lower surface. Comparisons are made with reference values in Table 1. It is found that our results agree well with those in Ref. [9]. Here, $\phi=180^\circ-\theta$, and $c=|\omega_r|/k$.

3. Numerical results

For the neutral mode ($\omega_i=0$), the Marangoni number Ma_N is a function of α,β,Pr,Q and Bi. The critical Marangoni number Ma_c can be defined as the global minimum of Ma_N for all (α,β),

$$Ma_c(Pr,Q,Bi)=\min_{\alpha,\beta}Ma_N(\alpha,\beta;Pr,Q,Bi). \tag{3.1}$$

This means that all modes are stable ($\omega_i<0$) at $Ma<Ma_c$. On the contrary, there are unstable modes ($\omega_i>0$) for some (α,β) when $Ma>Ma_c$. When $Q=0$, both the velocity and temperature distributions are symmetric with respect to the central plane z=0. We will discuss the cases at $Q=0$ and $Q>0$ separately. Our computation suggests that there are four kinds of preferred modes,

Table 1
Some critical parameters of the thermocapillary liquid layer with a single free surface. Here, "a" and "b" stand for the results of Ref. [9] and present work, respectively, while "..." means the data is not available.

Flow	*Pr*	*Bi*	*Ma*		*k*		ϕ		*c*	
			a	b	a	b	a	b	a	b
Linear flow	0.01	1	14.6	14.5	...	1.2	...	86°	...	0.0101
	100	0	15.6	15.62	0.73	0.725	90°	90°	0	0
Return flow	0.01	1	19.3	19.4	...	1.20	...	82°	...	0.0150
	100	0	376	375.3	2.50	2.48	7.6°	7.5°	0.0624	0.0622

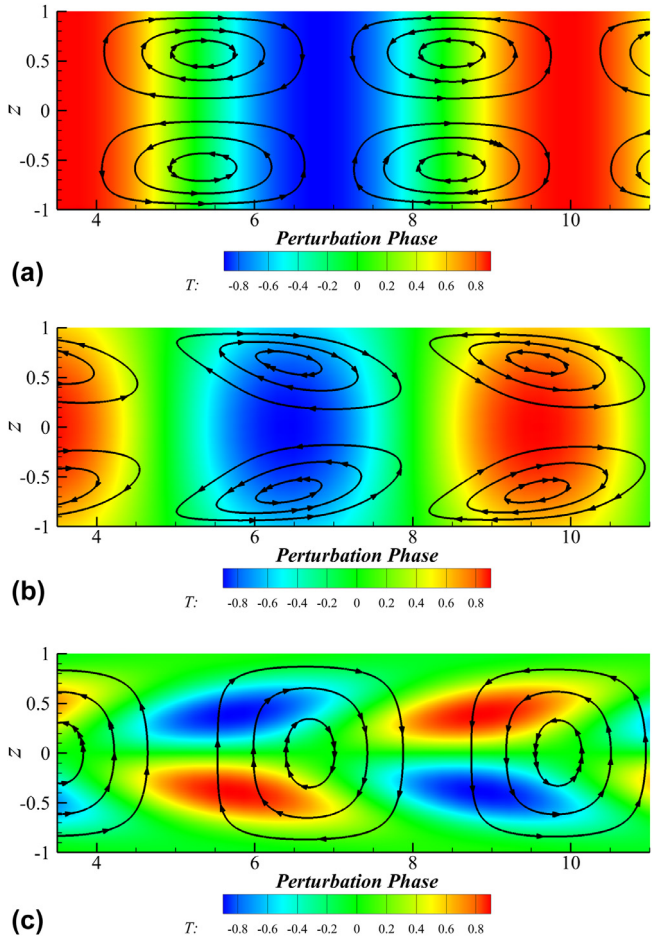

Fig. 5. The streamlines and isothermals of preferred modes at Q=0: (I) Pr=0.01, Bi=0; (II) Pr=0.01, Bi=1; (III) Pr=100, Bi=1.

which are the downstream streamwise wave ($\theta = 0°$), the upstream streamwise wave ($\theta = 180°$), the spanwise stationary mode ($\theta = 90°$, $\omega = 0$) and the upstream oblique wave ($\theta \in (90°, 180°)$).

3.1. $Q = 0$

The variation of Ma_c with Pr at Q=0 is displayed in Fig. 3. When Bi=0, there are two kinds of preferred modes, which are the upstream oblique wave ($\theta \in (90°, 180°)$ at Pr<1.1 and downstream streamwise wave (θ=0°) at Pr>1.1. Generally, Ma_c increases with Pr. However, there is a slight decrease of Ma_c at 1.1<Pr<1.4.

When Bi>0, Ma_c increases with Bi. However, the increase is more significant at small Pr. For example, when Pr=0.01, Ma_c increases from 2.01 at Bi=0 to 8.52 at Bi=1, while for Pr=100, Ma_c increases from 164 at Bi=0 to 181 at Bi=1. This property is similar to that of return flow [9]. For the preferred mode, the streamwise wave at large Pr changes from downstream [θ=0°, curves (b) & (e)] to upstream [θ=180°, curves (f) & (h)] when Bi increases.

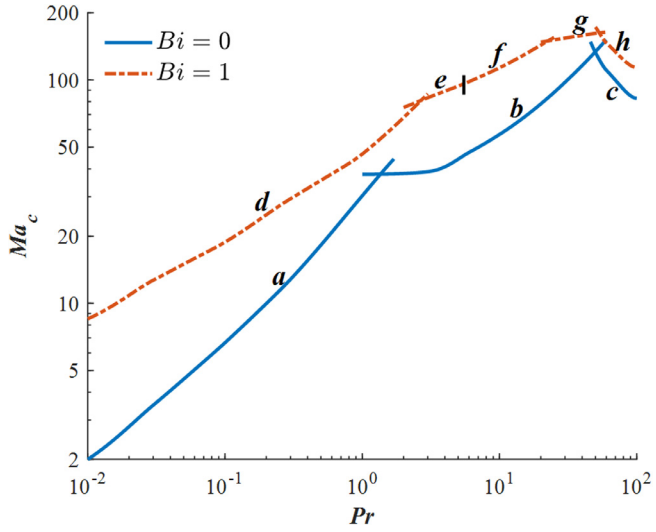

Fig. 6. The variation of Ma_c with Pr at Q=0.05.The curves correspond to oblique waves: (a), (d), (e); streamwise waves: (b), (f), (g); and spanwise stationary modes: (c), (h). Both axes are logarithmic.

The wave number k, propagation angle θ, wave speed c and frequency ω corresponding to the preferred modes in Fig. 3 are displayed in Fig. 4. It can be seen that when Bi=0, k, c and ω at large Pr are much larger than those at small Pr. For Bi=5, the propagation angle of oblique wave increases from θ=94° to θ=180° when Pr increases. On the contrary, the variation of θ with Pr is not obvious for the same mode at Bi=0 and Bi=1.

The streamlines and isothermals of preferred mode at Q=0 are plotted in Fig. 5. It can be seen that the symmetry of basic flow leads to the symmetry of perturbation. In Fig. 5 I & II, the perturbations at Pr=0.01 are symmetric with respect to the central plane z=0. There are four rolls in one cycle and the temperature changes little in the vertical direction. On the contrary, the perturbation is anti-symmetric at Pr=100 (Fig. 5 III). There are only two rolls in one cycle, and the amplitude of temperature appears in the interior of flow region. When Bi>0, the perturbation temperature near the surface decreases (Fig. 5 II & III) and the rolls at small Pr become oblique (Fig. 5 II).

3.2. $Q > 0$

The variation of Ma_c with Pr at Q=0.05 is displayed in Fig. 6. When Bi=0, there are three kinds of preferred modes, which are the upstream oblique wave at Pr<1.2, downstream streamwise wave at 1.2<Pr<49 and spanwise stationary mode (θ=90°, $\omega = 0$) at Pr>49. For small Pr, Ma_c increases with Pr, while the opposite case appears at large Pr. The preferred modes are similar to those in the linear flow for the liquid layer on the plane[9]. However, the streamwise wave of the latter is upstream(θ=180°), which is opposite to the case of curve (b) in Fig. 6. When Bi=1, there are two kinds of streamwise waves, which travel upstream[curve (f)] and downstream[curve (g)], and two kinds of oblique wave[curves (d) & (e)].

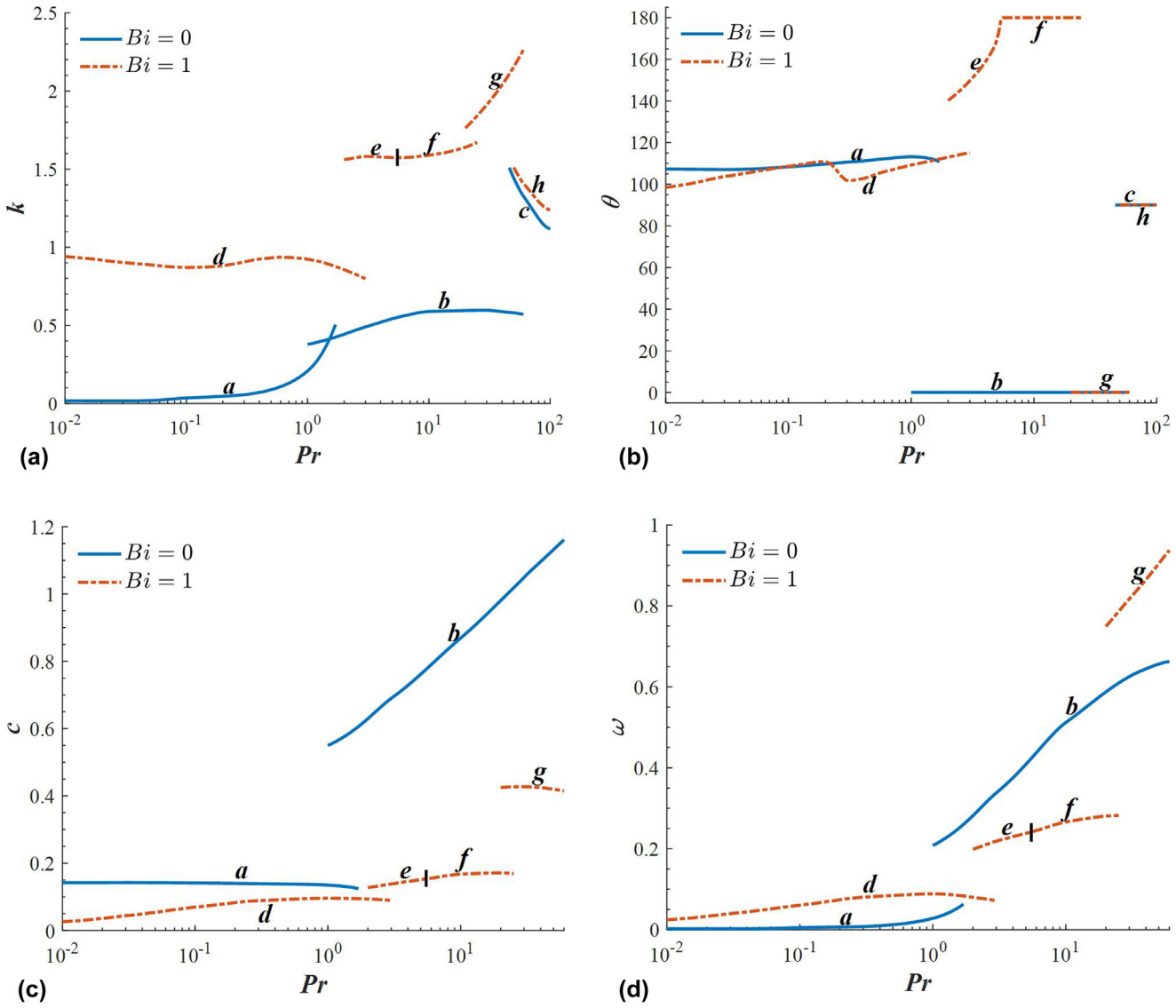

Fig. 7. The (I) wave number, (II) wave propagation angle, (III) wave speed and (IV) frequency corresponding to the modes in Fig. 6.

The wave number, propagation angle, wave speed and frequency corresponding to the preferred modes in Fig. 6 is displayed in Fig. 7. When $Pr<10$, k significantly increases with Pr at Bi=0. However, all wave numbers have the same order for all Pr at Bi=1. Generally, both c and ω increase with Pr for the oblique waves and streamwise waves.

The streamlines and isothermals of preferred modes at Q=0.05, Bi=0 are plotted in Fig. 8. For Pr=3 (Fig. 8 I), the hot spot appears on the free surface and there are two rolls in one cycle. For Pr=100 (Fig. 8 II), the hot spot is in the interior and there are four rolls in one cycle. However, due to the asymmetry of temperature distribution in the basic flow, the upper and lower rolls are not symmetric. The perturbation fields at small Pr are similar to the cases in Fig. 5.

It can be seen from the perturbation equations that Q is only related to $\frac{\partial T_0}{\partial z}$ in (2.14). Fig. 2 suggests that when $Q \geq 0.075$, the variation of T_b with z is monotonous, and a larger Q only leads to a larger temperature gradient. In addition, our computation shows that the critical modes at $Q > 0.05$ are similar to those at $Q \leq 0.05$ and there is no qualitative change for the instability. Thus, the results at larger Q are nor presented.

3.3. Energy analysis

We examine the energy growth of perturbation by the evolution equation of kinetic energy [16],

$$\frac{\partial E_k}{\partial t} = -\frac{1}{2R}\int(\boldsymbol{\tau}:\mathbf{S})d^3r + \frac{1}{R}\int \mathbf{u}\cdot\boldsymbol{\tau}\cdot\mathbf{n}d^2r - \int \mathbf{u}\cdot((\mathbf{u}\cdot\nabla)\mathbf{u}_0)d^3r = -N + M + I, \tag{3.2}$$

where N is the viscous dissipation, M is the work done by Marangoni forces on the surfaces and I is the energy from the basic flow. Here, $\int fd^2r$ and $\int fd^3r$ stand for the surface and volume integrals, respectively. In Table 2, we list the terms in (3.2) at different parameters, which are normalized by the kinetic energy $2E_k = \int|\mathbf{u}|^2d^3r = 1$.

It can be seen that when Bi=0, most of the perturbation energy comes from the Marangoni forces caused by perturbation temperature on the surfaces, while I is small enough to be neglected. However, when $Bi \geq 1$, I becomes the main energy source for the perturbation at Pr=0.01. The importance of I increases with Bi but decreases with Pr. The increase of Q has little effect on the energy mechanism.

Table 2
The terms in (3.2) for the preferred modes at different parameters.

	Pr	-*N*	*M*	*I*	Preferred mode
Q=0, *Bi*=0	100	-2.446421	2.453128	-0.006698	streamwise wave
	10	-0.789956	0.801094	-0.011134	
	1	-0.242951	0.242833	0.000119	oblique wave
	0.01	-0.037253	0.037222	0.000033	
Q=0, *Bi*=1	0.01	-0.004117	0.001158	0.002963	
Q=0, *Bi*=5	0.01	-0.002118	0.000201	0.001919	
Q=0.05, *Bi*=1	0.01	-0.004135	0.001157	0.002983	
Q=0.05, *Bi*=0	100	-16.492175	16.477791	0.014385	spanwise stationary mode
Q=0.05, *Bi*=1	100	-12.426678	12.407012	0.019669	

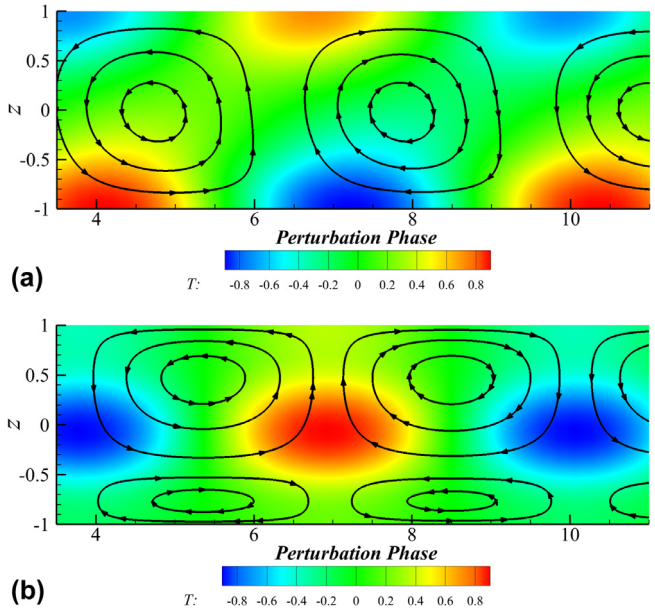

Fig. 8. The streamlines and isothermals of preferred modes at *Q*=0.05, *Bi*=0: (I) *Pr*=3; (II) *Pr*=100.

4. Discussion

In this section, first, we compare our results with the layer with a single free surface. Then, comparisons are made with numerical and experimental works. Finally, the instability mechanism is discussed.

4.1. Comparisons with the layer with a single free surface

The velocity distribution in Fig. 2 is similar to that of return flow [9]. In addition, the vertical temperature distribution at *Q*=0 in Fig. 3 indicates that the surface is hotter than the interior region, which is also the same as the case of return flow. So we would like to compare the layer at *Q*=0 with the return flow. When *Bi*=0, Ma_c of the latter is about three times that in Fig. 3 for fixed *Pr*. This is reasonable as the layer of return flow is placed on a rigid plane, which increases the constraint and stabilizes the flow. The wave number and frequency of the latter are also much larger than those of the former. Meanwhile, the downstream streamwise wave at large *Pr* [curves (b) & (e) in Fig. 3] cannot be found in the latter. For small *Pr*, the isothermals are nearly vertical lines in Fig. 5, which are the same as those of the latter [33]. In Table 2, *I* is negligible at small *Pr* at *Bi*=0. On the contrary, *I* is the main energy source for the latter[12,13].

When $Q > 0$, the temperature distribution in Fig. 3 suggests that the layer is heated from below, which is the same as the case of linear flow [9]. Three preferred modes in the linear flow (oblique wave, streamwise wave and spanwise stationary mode) are also detected in Fig. 6. However, the propagation directions of streamwise waves for two layers are opposite.

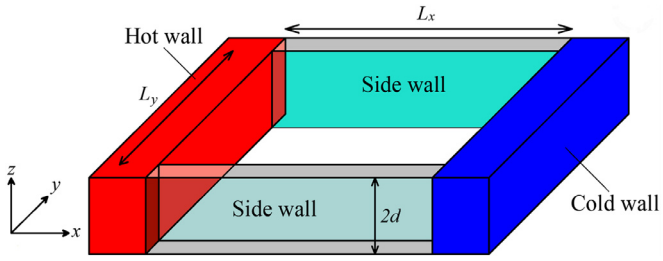

Fig. 9. The liquid film sustained in a rectangular hole.

4.2. Comparisons with numerical simulations and experiments

There have been some numerical and experimental works on the thermocapillary convection with the geometry shown in Fig. 9, where a liquid film with two free surfaces is sustained in a rectangular hole. L_x is the distance between the different temperature controlled end walls, while L_y is the distance between two side walls which are adiabatic. The flows with different aspect ratios ($L_x/2d$, L_y/L_x) have been examined with numerical and experimental approaches [26–28]. When L_x, $L_y >> 2d$, the flow away from walls corresponds to the case considered in Fig. 1. So we could make a comparison of our results with theses works.

The numerical simulation by Limsukhawat et al. [28] shows that the perturbation field at *Pr*=68.4, $L_x/2d$=6.67, L_y/L_x=1.5 is antisymmetric about the central plane, and the hot spots are in the interior of flow region. The distributions of perturbation temperature agree well with those in Fig. 5(c). However, the critical Marangoni number determined in the simulation has $Ma_c \approx 1900$, which is much larger than our results in Fig. 3. The reason may be attributed to the difference in their geometries. The layer in this paper is assumed to be infinite. However, the liquid film in the simulation is sustained in a hole with end walls in the streamwise and spanwise directions. As compared with the depth of the layer, the lengths in these two directions are not large enough. Thus, the constraints of end walls are obvious, which significantly increase Ma_c.

Watanabe, Kowata & Ueno [26] reported the experiment of thermocapillary liquid film for silicone oil of 5 cSt (*Pr*=68.4 at 25°C) at $L_x/2d$=3.33, L_y/L_x=6. It shows that $Ma_c \approx 368$, and the hydrothermal waves propagate steadily from the cold wall to the hot wall at $\theta \approx 15^\circ$, $k \sim 2.5$, $c \sim 0.15$, $f = \omega/(2\pi) \sim 0.06$. This corresponds to $\theta \approx 165^\circ$, $k \sim 1.25$, $c \sim 0.3$, $\omega \sim 0.375$ in our definition (we define the length scale as half the depth of the layer). The propagation angle is close to that at high *Pr* and *Bi*>0. Other parameters have the same orders as those in Fig. 4. The differences of critical parameters can be attributed to not only the geometry, but also the buoyancy effect in the experiment.

4.3. Instability mechanism

4.3.1. Q=0

For small *Pr*, the propagation angle $\theta \approx 90^{\circ}$. So we could consider the spanwise wave for simplicity. When *Bi*=0, the energy analysis indicates that the Marangoni force is crucial for the instability while the inertial effect of basic flow is negligible. Therefore, the key to the mechanism is the streamwise flow on the surface, which heats the hot spot by convection($u\frac{\partial T_0}{\partial x} < 0$). Here, $u>0$ for the hot spot on the surface, which is opposite to the case of return flow [33]. The heat diffusion and viscous dissipation can be significantly increased by the increase of wave number, which stabilizes the flow. Thus, *k* is very small for curve (a) in Fig. 4(I). When *Bi*>0, the perturbation temperature decreases while the importance of *I* increases. When *I* becomes the main energy source, the key to the mechanism changes to the inertial-driven streamwise flow [33], which has $u<0$ for the hot spot on the surface.

For large *Pr*, the instability is caused by the heat convection. The hot spot in the flow region is mainly heated by the streamwise convection (U_0T) at *Bi*=0 and the vertical convection ($w\frac{\partial T_0}{\partial z}$) at *Bi*>0 (see Fig. 5(III)). Then, the surface is heated by the interior hot spot by conduction and the Marangoni force drives the instability.

4.3.2. Q>0

For small *Pr*, the mechanism and perturbation flow field at $Q>0$ are similar to those at *Q*=0. For moderate *Pr*, Fig. 8(I) suggests that the key to the mechanism is the hot spot on the surface, which is heated by the streamwise convection ($u\frac{\partial T_0}{\partial x}$). It can be inferred that the temperature at the perturbation phase $\psi = 5$ will increase by the convection. This makes the wave travelling downstream.

For large *Pr*, it seems that the spanwise stationary mode is similar to the Marangoni convection in the layer heated from below. However, the temperature distribution in Fig. 8(II) is very different from that in the linear flow, which has vertical isothermals. This can be explained as follows. The convection of the lower vortices decreases the temperature below the hot spot. Meanwhile, $|\frac{\partial T_0}{\partial z}|$ is relatively small at $z>0$, thus the effect of vertical convection becomes weak. This is the reason why the perturbation of temperature is not obvious in the upper and lower region of the hot spot. Therefore, the instability is caused by the vertical convection in the interior and the heat conduction near the surfaces.

In many applications of non-isothermic liquid layers, such as solutions [34,35] and binary mixtures [36], the Marangoni stress induced by the concentration gradient is comparable to that caused by the temperature gradient. So the solutocapillary effect is also important for the convection. The instability becomes very complex due to the competing contributions of thermal and solutal Marangoni stress [37]. In crystal growth, the crystal can play an active role in coupled thermo-solutal capillary instabilities [38]. We plan to investigate the thermo-solutal capillary convection of double free-surface film in future works.

5. Conclusion

We examine the convective instability in the thermocapillary layer with two free surfaces by linear stability analysis. The parameters of preferred modes are obtained at different Prandtl numbers (*Pr*) and Biot numbers (*Bi*). The effect of vertical temperature difference between two interfaces (*Q*) is considered.

When *Q*=0, the preferred modes are the oblique wave at small *Pr* and the streamwise wave at large *Pr*. The former always travels upstream while the propagation direction for the latter depends on *Bi* and *Pr*. The perturbation flow fields at small *Pr* are symmetric with respect to the central plane. There are four rolls in one cycle and the perturbation temperature changes little in the vertical direction. On the contrary, the perturbation is antisymmetric at large *Pr*. There are only two rolls in one cycle and the amplitude of perturbation temperature appears in the interior of flow region. When *Bi*=0, the wave number, wave speed and frequency at large *Pr* are much larger than those at small *Pr*. The key to the mechanism is the streamwise convection. When *Bi*>0, the perturbation temperature on the surface decreases and the rolls become oblique. The instability is mainly caused by the inertial-driven streamwise flow at small *Pr* and the vertical convection at large *Pr*.

When *Q*>0, the preferred modes include the oblique wave at small *Pr*, the streamwise wave at moderate *Pr* and the spanwise stationary mode at large *Pr*. For *Bi*=0, the streamwise wave is downstream, while for *Bi*>0, it can be either upstream or downstream. Due to the asymmetry of temperature distribution in the basic flow, the perturbation fields are not symmetric. The hot spot is on the free surface at moderate *Pr* and in the interior of flow region at large *Pr*.

Energy analysis suggests that when *Bi*=0, the perturbation energy mainly comes from the Marangoni force while the energy from the basic flow (*I*) is negligible. When *Bi*>0, the importance of *I* increases with *Bi* but decreases with *Pr*. *I* becomes the main energy source for small *Pr* when *Bi* is large enough. The increase of *Q* has little effect on the energy mechanism.

Comparing the double free-surface layer with the single free-surface one, we can find that the temperature distribution of the former at *Q*=0 is similar to that of return flow. However, when *Bi*=0, the critical Marangoni number, wave number and frequency of the former are much smaller than those of the latter. In addition, their energy mechanisms at small *Pr* are totally different. The temperature distributions at *Q*>0 is more similar to that of linear flow. However, there are many differences in their instability mechanisms and perturbation flow fields.

Author Statement

Manuscript title: Instabilities of thermocapillary liquid layers with two free surfaces. I have made substantial contributions to the conception and the analysis of data for the work; and I have revised it critically for important intellectual content; and I have approved the final version to be published; and I agree to be accountable for all aspects of the work in ensuring that questions related to the accuracy or integrity of any part of the work are appropriately investigated and resolved. Cheng-Zhuo Zhao & Shao-Neng Zhang have made contributions to the data curation and validation. Qi-Sheng Chen have provided editing and writing assistance. The authors also gratefully acknowledge the referees for their many helpful comments in the Acknowledgment.

Declaration of Competing Interest

We declare that we have no financial and personal relationships with other people or organizations that can inappropriately influence our work, there is no professional or other personal interest of any nature or kind in any product, service and/or company that could be construed as influencing the position presented in, or the review of, the manuscript entitled.

Acknowledgments

This work has been supported by the National Natural Science Foundation of China (Nos.11872032 and 11772344), Zhejiang Provincial Natural Science Foundation (LY21A020006), K. C. Wong Magna Fund and the Special research funding from the Marine Biotechnology and Marine Engineering Discipline Group in Ningbo

University (No. 422004582). The authors also gratefully acknowledge the referees for their many helpful comments.

References

[1] T. Dufar, Crystal Growth Processes Based on Capillarity: Czochralski, Floating Zone, Shaping and Crucible Techniques, John Wiley & Sons, 2010.
[2] O.A. Basaran, H. Gao, P.P. Bhat, Nonstandard inkjets, Annu. Rev. Fluid Mech. 45 (2013) 85–113.
[3] W.Q. Dai, M.M. Khonsari, C. Shen, X. Wang, Thermocapillary migration of liquid droplets induced by a unidirectional thermal gradient, Langmuir 32 (30) (2016) 7485–7492.
[4] A. Karbalaei, R. Kumar, H. Cho, Thermocapillarity in microfluidics-a review, Micromachines 7 (2) (2016) 1–41 13.
[5] K.N. Kowal, S.H. Davis, P.W. Voorhees, Thermocapillary instabilities in a horizontal liquid layer under partial basal slip, J. Fluid Mech. 855 (2018) 839–859.
[6] S.H. Davis, Thermocapillary instabilities, Annu. Rev. Fluid Mech. 19 (1) (1987) 403–435.
[7] M.F. Schatz, G.P. Neitzel, Experiments on thermocapillary instabilities, Annu. Rev. Fluid Mech. 33 (1) (2001) 93–127.
[8] M. Lappa, Thermal Convection: Pattern, Evolution and Stability, John Wiley and Sons, Inc., Chichester, 2010.
[9] M.K. Smith, S.H. Davis, Instabilities of dynamic thermocapillary liquid layers. Part 1.Convective instabilities, J. Fluid Mech. 132 (1983) 119–144.
[10] R.J. Riley, G.P. Neitzel, Instability of thermocapillary–buoyancy convection in shallow layers. Part 1. Characterization of steady and oscillatory instabilities, J. Fluid Mech. 359 (1998) 143–164.
[11] Y.R. Li, N. Imaishi, T. Azami, T. Hibiya, Three-dimensional oscillatory flow in a thin annular pool of silicon melt, J. Cryst. Growth 260 (2004) 28–42.
[12] M. Wanschura, V. Shevtsova, H. Kuhlmann, H. Rath, Convective instability mechanisms in thermocapillary liquid bridges, Phys. Fluids 7 (1995) 912–925.
[13] C.Y. Yan, K.X. Hu, Q.S. Chen, Thermocapillary instabilities of liquid layers on an inclined plane, Phys. Fluids 30 (8) (2018) 082101.
[14] M.K. Smith, S.H. Davis, Instabilities of dynamic thermocapillary liquid layers. part 2. surface-wave instabilities, J. Fluid Mech. 132 (1983) 145–162.
[15] R. Patne, Y. Agnon, A. Oron, Thermocapillary instabilities in a liquid layer subjected to an oblique temperature gradient, J. Fluid Mech. 906 (A12) (2021) 1–30.
[16] K.X. Hu, M. He, Q.S. Chen, Instability of thermocapillary liquid layers for Oldroyd-B fluid, Phys. Fluids 28 (3) (2016) 033105.
[17] K.X. Hu, M. He, Q.S. Chen, R. Liu, Linear Stability of Thermocapillary Liquid Layers of a Shear-thinning Fluid, Phys. Fluids 29 (2017) 073101.
[18] K.X. Hu, M. He, Q.S. Chen, R. Liu, Effect of Gravity on the Stability of Viscoelastic Thermocapillary Liquid Layers, Int. J. Heat Mass Transfer 123 (2018) 776–786.
[19] K.X. Hu, M. He, Q.S. Chen, R. Liu, On the Stability of Thermocapillary Convection of a Bingham Fluid in an Infinite Liquid Layer, Int. J. Heat Mass Transfer 112 (2018) 993–1002.
[20] K.X. Hu, S. Zheng, Q.S. Chen, Transient growth in thermocapillary liquid layers, Phys. Rev. Fluids 5 (2020) 014001.
[21] K.X. Hu, C.Y. Yan, Q.S. Chen, Instability of thermocapillary-buoyancy convection in droplet migration, Phys. Fluids 31 (2019) 122101.
[22] L.A. Davalos-Orozco, Sideband thermocapillary instability of a thin film flowing down the outside of a thick walled cylinder with finite thermal conductivity, Int. J. Non-Linear Mech. 109 (2019) 15–23.
[23] L. Zhang, Y.R. Li, C.M. Wu, Q.S. Liu, Flow bifurcation routes to chaos of thermocapillary convection for low prandtl number fluid in shallow annular pool with surface heat dissipation, Int. J. Therm. Sci. 125 (2018) 23–33.
[24] Q. Kang, J. Wang, L. Duan, Y. Su, J. He, D. Wu, W. Hu, The volume ratio effect on flow patterns and transition processes of thermocapillary convection, J. Fluid Mech. 868 (2019) 560–583.
[25] D. Pettit, Saturday Morning Science Videos, see http://mix.msfc.nasa.gov/IMAGES/QTVR/0601211.mov (2003).
[26] T. Watanabe, Y. Kowata, I. Ueno, Flow transition and hydrothermal wave instability of thermocapillary-driven flow in a free rectangular liquid film, Int. J. Heat Mass Transfer 116 (2018) 635–641.
[27] I. Ueno, T. Torii, Thermocapillary-driven flow in a thin liquid film sustained in a rectangular hole with temperature gradient, Acta Astronaut 66 (7-8) (2010) 1017–1021.
[28] D. Limsukhawat, Y. Dekio, K. Ikebukuro, Ueno Hong, Flow patterns induced by thermocapillary effect in a thin free liquid film of a high Prandtl number fluid, Prog. Comput. Fluid Dy. 13 (3-4) (2013) 132–140.
[29] B. Messmer, T. Lemee, K. Ikebukuro, I. Ueno, R. Narayanan, Confined thermo–capillary flows in a double free-surface film with small marangoni numbers, Int. J. Heat Mass Transfer 78 (2014) 1060–1067.
[30] T. Yamamoto, Y. Takagi, Y. Okano, S. Dost, Numerical investigation for the effect of the liquid film volume on thermocapillary flow direction in a thin circular liquid film, Phys. Fluids 25 (8) (2013) 489–500.
[31] T. Yamamoto, Y. Takagi, Y. Okano, S. Dost, Numerical investigation of oscillatory thermocapillary flows under zero gravity in a circular liquid film with concave free surfaces, Phys. Fluids 28 (3) (2016) 032106.
[32] P.J. Schmid, D.S. Henningson, Stability and Transition in Shear Flows, Springer, 2001.
[33] M.K. Smith, Instability mechanisms in dynamic thermocapillary liquid layers, Phys. Fluids 29 (10) (1986) 3182–3186.
[34] D.C. Venerus, D.N. Nieto, Tears of wine: new insights on an old phenomenon, Sci. Rep 5 (1) (2015) 16162.
[35] E. Bormashenko, R. Pogreb, O. Stanevsky, Y. Bormashenko, T. Stein, O. Gendelman, Mesoscopic patterning in evaporated polymer solutions: new experimental data and physical mechanisms, Langmuir 21 (2005) 9604–9609.
[36] A. Cröll, A. Mitric, O. Aniol, S. Schütt, P. Simon, Solutocapillary convection in germanium-silicon melts, Cryst. Res. Technol. 44 (10) (2009) 1101–1108.
[37] H. Minakuchi, Y. Takagi, Y. Okano, S. Gima, S. Dost, The relative contributions of thermo-solutal Marangoni convections on flow patterns in a liquid bridge, J. Cryst. Growth 385 (2014) 61–65.
[38] D. Schwabe, Convective instabilities in complex systems with partly free surface, J. Phy. Conf. Ser. 64 (1) (2007) 012001.